THE JOURNAL OF PHYSICAL CHEMISTRY C
A JOURNAL OF THE AMERICAN CHEMICAL SOCIETY

pubs.acs.org/JPCC

Article

Mapping of Grain Orientation *In Situ* of 2D Perovskite Thin Films with Low-Frequency Polarized Raman Microspectroscopy

Published as part of The Journal of Physical Chemistry virtual special issue "Kankan Bhattacharyya Festschrift".

Shogo Toda, Eric Wei-Guang Diau, and Shinsuke Shigeto*

Cite This: *J. Phys. Chem. C* 2021, 125, 27996–28003

Read Online

ACCESS | Metrics & More | Article Recommendations | Supporting Information

ABSTRACT: Recent developments in two-dimensional (2D) Ruddlesden–Popper perovskites have ushered in a new phase in optoelectronics through their promising physical, chemical, and optical properties. Thin films of 2D perovskites used in most optoelectronic applications contain many grains oriented either horizontally or vertically with respect to the substrate on which they grow; the orientation of such grains plays important roles, not yet fully understood, in their functionalities. Techniques to map the grain orientation *in situ* in 2D perovskite thin films are hence highly desirable. Here we report mapping of the grain orientation of thin films of the horizontal 2D perovskite, BA_2PbI_4, in which BA is butylammonium, with low-frequency polarized Raman microspectroscopy. We established a relation between the intensities of low-frequency (10–60 cm^{-1}) polarized Raman lines of BA_2PbI_4 originating primarily from the PbI_6 octahedra and varied orientations of a plate-like BA_2PbI_4 single crystal. This relation served to determine unambiguously the orientation of grains of micrometer size in a spin-coated BA_2PbI_4 thin film. Although this study is a case study of BA_2PbI_4, it opens a new window to obtain crystallographic information about 2D perovskite thin films in general and hence to understand their properties and functions.

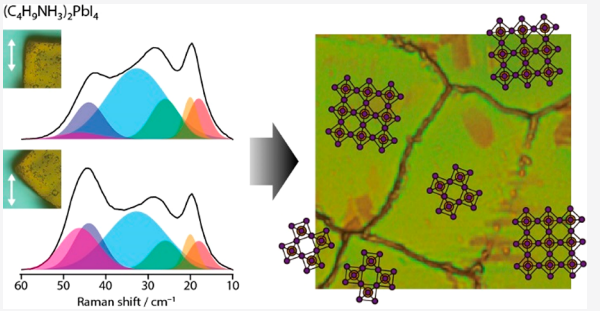

INTRODUCTION

Two-dimensional (2D) lead halide perovskites have generated much attention in recent years as hybrid materials with prospective applications in optoelectronics such as solar cells, light-emitting diodes, and photodetectors.[1−5] They exhibit improved stability against moisture,[6] great compositional and structural versatility,[4,7] strong confinement effects,[8,9] and superior solution processability[10,11] compared with their three-dimensional (3D) counterparts. Many outstanding properties of 2D perovskites stem from their unique crystal structures. In 2D perovskites, inorganic sheets of corner-sharing PbX_6 (X = Cl, Br, or I) octahedra are separated by interdigitating bilayers of bulky organic cations. By virtue of this layered nature, thin films of 2D perovskites, a desirable form for optoelectronic applications, tend to grow with individual planar grains oriented horizontally or vertically with respect to a substrate, depending on the number, *n*, of adjacent inorganic layers.[2,7,12,13] Grains and grain boundaries affect profoundly the physical properties of polycrystalline 2D perovskite thin films (e.g., charge mobility and density[14,15]) and consequently their optoelectronic device performances. To assess the grain orientation *in situ* in 2D perovskite thin films is thus vitally important.

Several imaging microscope techniques have been employed to obtain information about the crystallographic orientation of polycrystalline materials in a nondestructive manner. X-ray diffraction microscopy can map the grain orientation in 3D, but its spatial resolution is typically ∼10 μm when using a laboratory X-ray source.[16] To achieve imaging with sub-micrometer spatial resolution, synchrotron radiation is necessary,[17] which is available at only few facilities. Transmission electron microscopy (TEM) is also capable of 3D orientation mapping on a nanometer scale.[18,19] The samples feasible with this method are, however, restricted to foils of thickness several hundred nanometers; if a sample is too thick, the electron beam passes through multiple grains, making difficult an analysis of a diffraction pattern. Electron backscattering diffraction (EBSD), another widely used technique for orientation mapping,[20,21] is extremely susceptible to surface conditions and typically requires skilled sample preparation, such as cutting, grinding, and polishing of a sample.[22] Moreover, as TEM and EBSD must be performed under

Received: September 28, 2021
Revised: December 7, 2021
Published: December 21, 2021

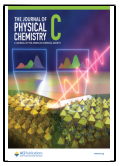

high vacuum, mapping of grain orientation at ambient pressure is infeasible.

Polarized Raman microscopy offers an optical alternative to mapping of grain orientation based on X-ray and electron diffraction. Tesar and colleagues[23] showed that polarized Raman microscopy of the phonon modes of GaV_4S_8 enabled determination of a cubic grain orientation, which was confirmed with EBSD. Ilchenko and colleagues[24] demonstrated the power of polarized Raman microscopy for 2D and 3D orientation mapping using polycrystalline Si, a pharmaceutical tablet containing carbamazepine (antiepileptic drug), and polycrystalline sapphire. We applied low-frequency polarized Raman (LFPR) microspectroscopy to map the *relative* grain orientation of thin films of a prototypical 2D Ruddlesden−Popper perovskite, BA_2PbI_4 (BA = $CH_3(CH_2)_3NH_3$).[25] BA_2PbI_4, being a single-layered (n = 1) 2D perovskite, adopts an intuitive horizontal orientation, rather than a vertical orientation, of its thin films.[2,7,12,13] We visualized intra- and intergrain inhomogeneity in BA_2PbI_4 thin films.

Here, we extended our previous work to mapping of *absolute* grain orientation, accomplished on examining the relation in space-fixed coordinates between the linear polarizations of the incident and Raman-scattered light and the orientation of a BA_2PbI_4 single-crystal flake. Raman images of the ultralow-frequency (<60 cm^{-1}) phonon lines in a series were then acquired on rotating a BA_2PbI_4 thin-film sample relative to the space-fixed frame, enabling us to determine the orientation of individual grains of micrometer size in that thin film. This work highlights the promising potential of LFPR microspectroscopy toward mapping of grain orientation not only of buried perovskite layers in real optoelectronic devices (e.g., solar cells) but also of mixed 2D/3D perovskites.[26−28]

EXPERIMENTAL SECTION

Synthesis of BA_2PbI_4. BA_2PbI_4 2D perovskite crystals were synthesized according to the reported procedures.[29,30] Briefly, PbO powder (Alfa Aesar, 10 mmol) was dissolved in a mixture of HI (57%, Alfa Aesar, 10 mL) and H_3PO_2 (50%, aqueous, Alfa Aesar, 1.7 mL) at room temperature. The clear-yellow solution was kept boiling for ∼5 min. *n*-Butylamine (924 μL, 10 mmol, Sigma-Aldrich) neutralized with excess HI (5 mL) was added dropwise to the boiling PbI_2 solution. After the solution became clear, stirring and heating the solution were stopped; the solution was left to cool to room temperature. The obtained orange flakes (Figure S1a) were collected by suction filtration and dried under low pressure at room temperature for a few days.

Film Fabrication. The synthesized BA_2PbI_4 was dissolved in dimethylformamide (DMF, anhydrous, FUJIFILM Wako) to yield a solution (45 mass %) of BA_2PbI_4. The solution was heated to 70 °C with stirring for 3 h, followed by filtration with a polytetrafluoroethylene (PTFE) filter (0.45 μm). The resulting solution (40 μL) was spin-cast onto a glass coverslip, treated with O_2 plasma, at 4000 rpm for 15 s. The BA_2PbI_4 thin film was then annealed at 100 °C on a Petri dish for 10 min. After heating, DMF (20 μL) was dropped around the perovskite film, producing DMF vapor inside the covered Petri dish. The perovskite film exposed to the DMF vapor was maintained at 100 °C for another 10 min, during which the growth of larger grains of the perovskite was promoted (solvent annealing[31]). The film was finally left for 1 min without the cover so that DMF was completely removed (see Figure S1b for the fabricated film). All these procedures were done in a glovebox filled with N_2.

LFPR Microspectroscopy and Imaging. Space-resolved polarized Raman spectra in the ultralow-frequency region of BA_2PbI_4 flakes and thin films were measured with a home-built confocal Raman microspectrometer (Figure S2 shows a schematic of the apparatus), described previously.[25,32] The output of a He−Ne laser at 632.8 nm served as the light source for Raman excitation. After passing through a half-wave plate and a Glan−Thompson polarizer to control the polarization, the laser beam was introduced to an inverted microscope (Nikon, TE2000-U, customized) using a volume Bragg grating (VBG) notch filter (OptiGrate, OD = 3) and a dichroic mirror, and focused onto the sample by an objective (100×, NA = 0.90, Nikon, Plan Apo Fluor). The laser power at the sample point was adjusted to be as little as 0.4 mW throughout the present work. The sample was placed on a three-axis piezoelectric nanopositioner (Mad City Laboratories, Nano-LP100) mounted on the microscope stage. Backscattered light was collected by the same objective. The well-collimated scattered light was passed through two more VBGs, which rejected almost all Rayleigh scattering with an extremely narrow width.[33−35] With these VBGs, ultralow-frequency Raman spectra down to ∼10 cm^{-1} were observed. The scattered light was then focused onto a 100 μm pinhole to achieve confocal detection. Another Glan−Thompson polarizer served as an analyzer. The transmitted light was analyzed by an imaging spectrometer (SOL Instruments, MS3501i) and detected with an electron-multiplying charge-coupled device (EMCCD) as detector (Andor Technology, Newton). The use of a grating (1800 mm^{-1}) resulted in spectral resolution 2 cm^{-1}. To suppress the influence of the polarization properties of the grating on the signal intensity, a quarter-wave plate as an effective depolarizer was installed between the analyzer and the focusing lens in front of the entrance slit of the spectrometer.

In the LFPR measurement of a BA_2PbI_4 single crystal, a 10 s exposure time was used. In LFPR imaging, the thin film sample was translated with the piezoelectric stage in a raster manner. An area of 30 μm × 30 μm was scanned at interval 1 μm. In total 31 × 31 = 961 LFPR spectra were thus acquired; the exposure time at each point was 1 s in this case. The spatial resolutions in the lateral (XY) and axial (Z) directions were estimated to be 0.90 and 4 μm, respectively. The polarization configuration was set to be $Z(YY)Z$ (in Porto notation[36]), for which the propagation directions of the incident and scattered light were along the Z-axis and their polarization directions were along the Y-axis (see Figure 1a). All measurements were done at room temperature.

Spectral Analysis. LFPR imaging data were subjected to noise reduction using singular value decomposition[37−39] (SVD). The largest 10 singular components were retained to reconstruct denoised data; the rest were discarded as noise. The baseline of each SVD-treated spectrum was then fit to a quadratic function and subtracted from the spectrum. These and other spectral analyses were performed on Igor Pro 8 (WaveMetrics).

RESULTS AND DISCUSSION

To determine precisely the relation between crystal orientation and the LFPR pattern, we first analyzed the LFPR spectra of a plate-like single crystal of BA_2PbI_4 measured at 45 varied angles ϕ; here ϕ is the angle between the space-fixed Y-axis (red double arrows in Figure 1a−h) and one distinct straight

https://doi.org/10.1021/acs.jpcc.1c08533
J. Phys. Chem. C 2021, 125, 27996−28003

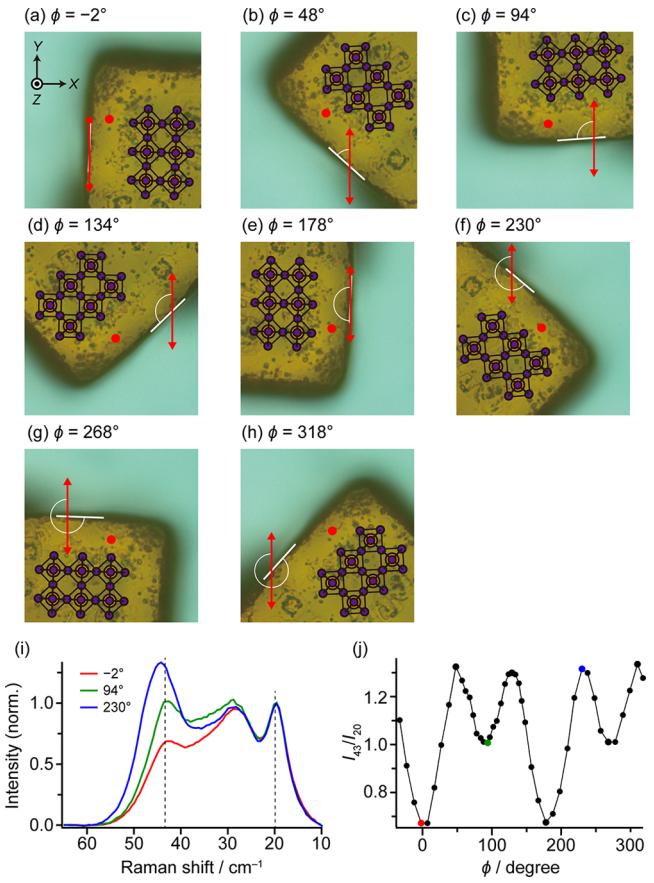

Figure 1. (a–h) Optical micrographs of a plate-like BA_2PbI_4 single crystal at $\phi = -2°$ (a), 48° (b), 94° (c), 134° (d), 178° (e), 230° (f), 268° (g), and 318° (h). Space-fixed coordinates *X*, *Y*, and *Z* are given in (a). Red double arrows and white lines represent the *Y*-axis and one straight edge of the BA_2PbI_4 flake, respectively. The octahedral lattice is schematically shown in each panel. Red circles indicate the positions at which the LFPR spectra were recorded. (i) Baseline-corrected LFPR spectra at three angles $\phi = -2°$ (red), 94° (green), and 230° (blue), normalized to peak height at 20 cm^{-1}. (j) Dependence on angle ϕ of the ratio of intensity at 43 cm^{-1} to that of 20 cm^{-1}, I_{43}/I_{20}. Colored circles highlight the three angles shown in (i).

edge of the rotated BA_2PbI_4 flake (white lines in Figure 1a–h), with positive ϕ defined as a counterclockwise rotation from the *Y*-axis. The angle was varied on rotating the crystal in the plane of the microscope stage (i.e., the *XY*-plane). Figure 1a–h displays optical micrographs of the crystal at $\phi = -2°$, 48°, 94°, 134°, 178°, 230°, 268°, and 318° as examples, respectively. With reference to BA_2PbBr_4,[40] which belongs to the same orthorhombic space group *Pbca* as BA_2PbI_4,[41,42] the edges of BA_2PbI_4 flakes are expected to be parallel to the directions of the main axes of the pseudocubic octahedral layer (see Figure 1a–h). We thereby related the LFPR spectrum measured at each angle to the crystal orientation of the BA_2PbI_4 flake. The normalized *Z*(*YY*)*Z* LFPR spectra at these orientations vary considerably depending on ϕ (see Figure 1i for spectra at three out of the eight angles shown in Figure 1a–h). The ratio of the intensity at 43 cm^{-1} to that at 20 cm^{-1}, I_{43}/I_{20}, took a maximum value ∼1.3 when the edge of the crystal was near diagonal ($\phi = 230°$) to the *Y*-axis. In contrast, I_{43}/I_{20} decreased as the incident light polarization became perpendicular (ϕ = 94°) and parallel ($\phi = -2°$) to the *Y*-axis. This ϕ-dependent periodic change of I_{43}/I_{20} is more evident in Figure 1j.

Although the orientation of the octahedral lattice is similar for the parallel and perpendicular configurations, the values of I_{43}/I_{20} differ (∼0.7 vs ∼1.0; see Figure 1j). This result indicates that the ϕ dependence of the LFPR spectral pattern must be interpreted in terms of the underlying lattice phonon modes. We therefore sought to decompose the LFPR spectra into individual lines, as previously.[25] The average of 45 normalized LFPR spectra (Figure 2a, upper panel) and its second

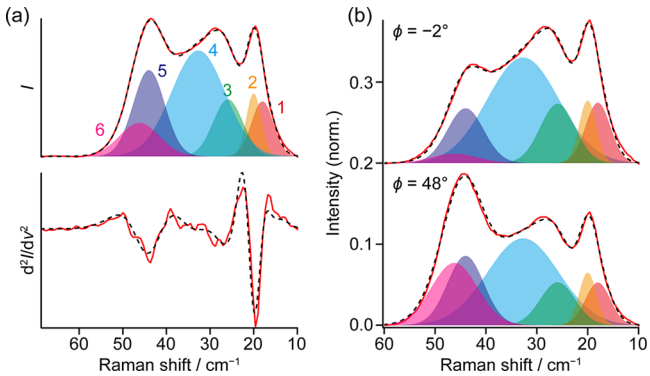

Figure 2. (a) Average normalized LFPR spectra measured at 45 angles ϕ (red solid line, upper panel) and its second derivative (red solid line, lower panel). Best fits obtained by using six Gaussian lines 1–6 are shown as black dashed lines. (b) Decomposition of LFPR spectra at $\phi = -2°$ and 48° into six Gaussian lines. Red solid lines and black dashed lines represent normalized LFPR spectra and best fits, respectively. The result for $\phi = -2°$ is offset by +0.2 for clarity.

derivative (Figure 2a, lower panel) were fit simultaneously by using six Gaussian functions (denoted lines 1–6 in order of increasing wavenumber). The peak positions of the six Gaussian lines were adopted from previous work,[25] whereas their widths were set as free parameters. The line widths obtained in the present fit are given in Table S1, with the peak positions fixed in advance. The satisfactory quality of the fit is illustrated in Figure 2b for $\phi = -2°$ and 48°. The present spectral decomposition can be rationalized in part by the fact that the minimum number of lines required to reproduce all 45 LFPR spectra well was six. The reported Raman spectra of BA_2PbX_4 (X = Br or I) at cryogenic temperatures[40,43] show at least five major signals below ∼60 cm^{-1}, which have been assigned, on the basis of density functional theory, to octahedral twisting and Pb–X bending modes.[44] The presence of one more mode in this work than in the literature might be due to the varied experimental conditions (e.g., measurement temperature, polarization configuration, and sample morphology).

Using Gaussian lines 1–6, we fit all normalized LFPR spectra at 45 angles ϕ in the same manner as above. Figure 3a plots the resulting area intensities, *I*, of lines 1–6 as a function of ϕ. From this figure, lines 1–6 clearly all exhibit a periodic dependence on ϕ. Among them, the ϕ dependences of lines 4 and 6 appear to be expressible with a single cosine function, which reflects the periodic change in the angle between the main axes of the octahedral lattice and the polarization direction of the excitation light. As shown in Figure 3b, the area intensities of lines 4 and 6 fit exceptionally well with the equation

https://doi.org/10.1021/acs.jpcc.1c08533
J. Phys. Chem. C 2021, 125, 27996–28003

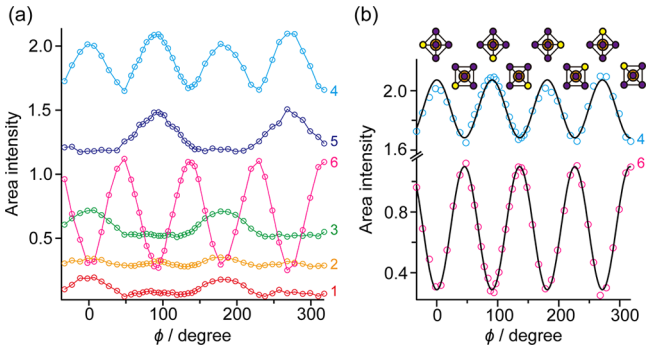

Figure 3. (a) Dependence on ϕ of area intensities of lines 1−6 derived from the LFPR spectral decomposition using six Gaussian lines (see Figure 2b). To facilitate comparison, the curve for line 5 is offset by +0.6. (b) ϕ-dependent area intensities of lines 4 and 6 (open circles) and best fits to eq 1 (black lines). The fitting parameters y_0, A, f_0, and α are respectively determined to be 1.88, 0.19, 0.069, and −1.0° for line 4 and 0.69, 0.41, 0.069, and 179.0° for line 6. To show explicitly the corresponding crystal orientation, we included in the figure the PbI_6 octahedra (top view) with one iodine atom highlighted in yellow.

$$I(\phi) = y_0 + A\cos(f_0\phi + \alpha) \quad (1)$$

in which y_0 is a ϕ-independent term, A is the amplitude, f_0 is the reciprocal of the angular period, and α is the phase in the space-fixed coordinate system. As expected from the symmetry of the octahedral lattice, f_0 is obtained to be ∼0.07 (= π/45°) for both lines. α is determined to be −1.0° for line 4 and 179.0° for line 6. The slight deviation from 0 and 180° is likely due to uncertainties of polarizations. The observed single cosinusoidal behavior implies that the lattice phonon modes that produce lines 4 and 6 have in-plane (XY) symmetry. The non-cosinusoidal ϕ dependences of the other lines could result from symmetry breaking induced by the BA^+ cation.[40] Because line 6 has a larger amplitude than line 4, we focused on line 6 in the following mapping of grain orientation of a thin film of BA_2PbI_4.

Having established the relation between the orientation of the BA_2PbI_4 crystal and LFPR spectra, we set out to assess quantitatively the orientation of individual grains constituting a thin film of the 2D perovskite. We performed $Z(YY)Z$ LFPR imaging on area 30 μm × 30 μm of the BA_2PbI_4 thin film fabricated on a glass coverslip (Figure 4a). Six grains (see below) were found in this region. In total, 961 LFPR spectra were fit to a linear combination of the same Gaussian lines 1−6 as those used in Figure 2. The decomposition results at positions i−iii belonging to separate grains (Figure 4b) show that the six-component model reproduces the LFPR spectra of the BA_2PbI_4 thin film as well as those of the single crystal (Figure 2). As in our previous work,[25] the Raman images of lines 1−6 (Figure 4c−h), which were constructed by using area intensity, distinctively visualize the grains. The Raman image of line 6 is in best agreement with the grain distribution seen in the optical micrograph (Figure 4a). On inserting the area intensity of line 6 determined for each grain into eq 1, we might deduce its absolute orientation, but as illustrated in Figure S3a, it is impracticable to distinguish between two crystal orientations (one making angle $+\alpha$ with the Y-axis and the other making angle $-\alpha$ with the Y-axis) solely from imaging results at one orientation of the film. Because these orientations exhibit opposite changes in the line intensity

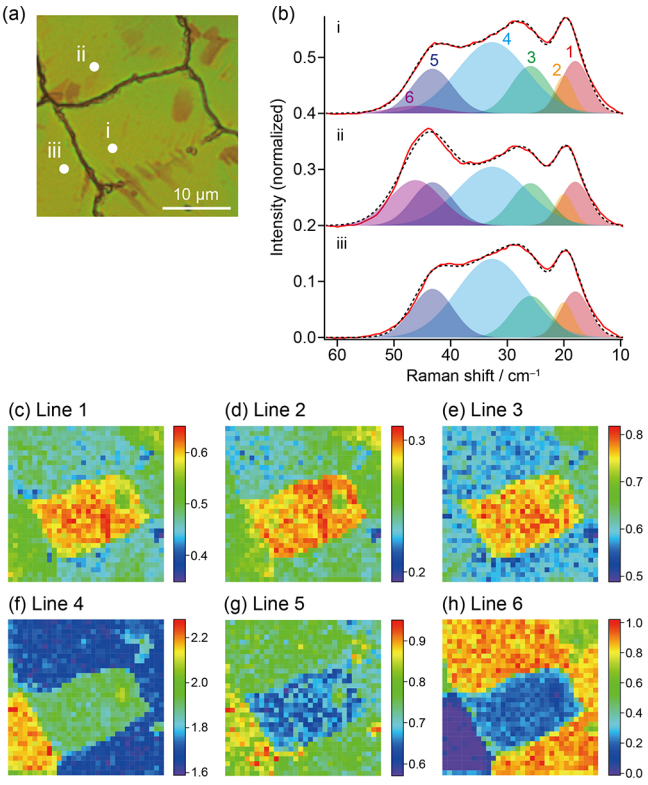

Figure 4. (a) Optical micrograph of area 30 μm × 30 μm of a thin film of BA_2PbI_4 fabricated on a glass coverslip. Scale bar = 10 μm. (b) Line decomposition results of the $Z(YY)Z$ LFPR spectra at positions i−iii indicated in (a). Each spectrum is offset for clarity of display. (c−h) Raman images of lines 1 (c), 2 (d), 3 (e), 4 (f), 5 (g), and 6 (h) in rainbow pseudocolor, with the greatest and least intensities coded in red and purple, respectively.

(either increase or decrease) when a film is rotated (see Figure S3b), LFPR imaging at varied film orientations would resolve this problem.

To that end, we repeated LFPR imaging at eight other film orientations (θ = 18°, 24°, 33°, 40°, 50°, 61°, 74°, and 85°; see Figure 5) on rotating the thin-film sample counterclockwise by angle θ with respect to the orientation shown in Figure 5a (defined as θ = 0°). As the film was rotated, the pseudocolor of the grains altered greatly, reflecting the change of the grain orientation relative to the direction of the light polarization (Y). For example, grain A, located at the center of the image, changed its pseudocolor from purple (representing a low intensity of line 6) at θ = 18°, to green (medium intensity) at 40°, to red (high intensity) at 61°, and eventually to green again at 85°. Similar changes were also observed for other grains B−F.

To investigate quantitatively how the intensity of line 6 in each grain varied with θ, we determined regions of interest (ROI) inside each grain A−F (see Figure S4) and obtained a representative value of the intensity of line 6 for each grain on averaging the intensities in the ROI. Figure 6 plots the representative intensity values of line 6 for grains A−F as a function of θ (open circles). The small error bars ensure that the intensity variation within the ROI is not large and that the values shown in Figure 6 are indeed representative of each grain. Just like Figure 3b, the dependence on θ of each grain was fit individually (dashed lines) by using eq 2:

https://doi.org/10.1021/acs.jpcc.1c08533
J. Phys. Chem. C 2021, 125, 27996−28003

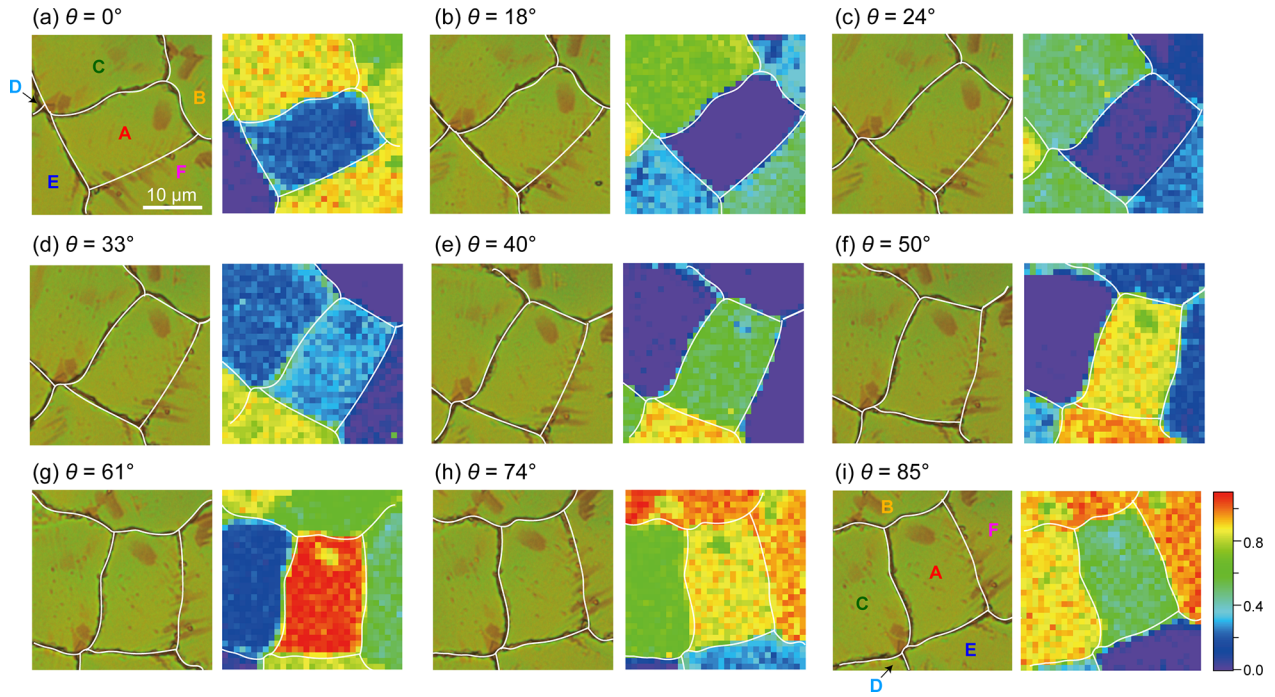

Figure 5. Optical micrographs (left) and Raman images of lines 6 (right) of a thin film of BA_2PbI_4 at $\theta = 0°$ (a), 18° (b), 24° (c), 33° (d), 40° (e), 50° (f), 61° (g), 74 (h), and 85° (i). We defined the orientation of (a) (the same image as Figure 4a) as $\theta = 0°$ and calculated the value of θ on examining the direction of a straight part of the grain boundary. The six grains found in the scanned area are labeled A−F. Grain boundaries were visually identified from the optical micrographs and are depicted as white lines in both optical micrographs and Raman images. As in Figure 4c−h, Raman images are shown in rainbow pseudocolor. The same color scale applies to all Raman images. Scale bar = 10 μm.

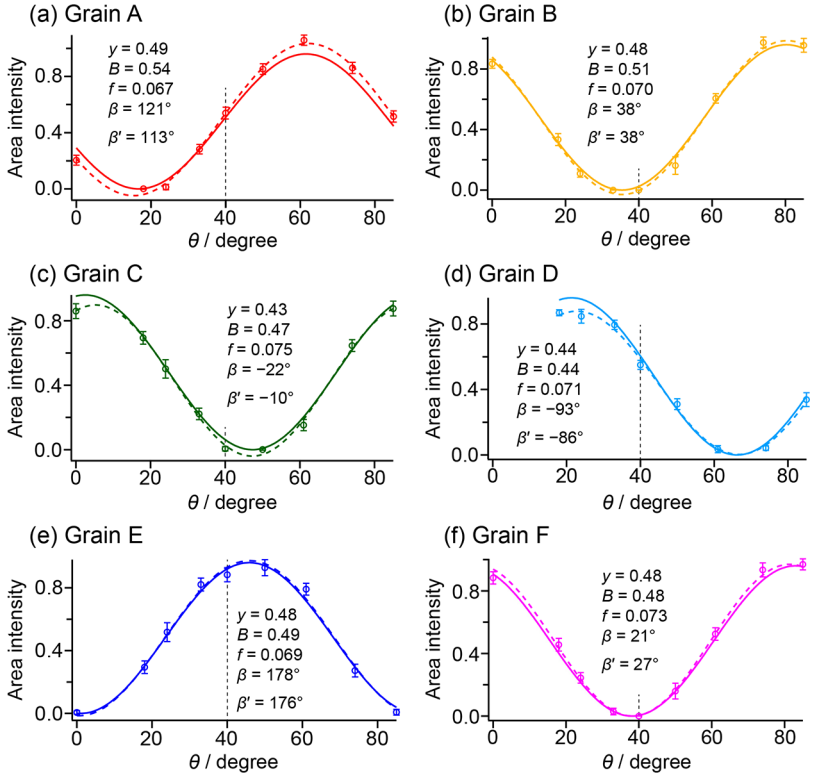

Figure 6. Area intensities of line 6 for grains A (a), B (b), C (c), D (d), E (e), and F (f) plotted as a function of θ. Data represent mean ± standard deviation (calculated for each ROI shown in Figure S4). Dashed and solid lines show fits to eqs 2 and 3, respectively. The determined parameters (y, B, f, β, and β') are provided with the fits. The data point at $\theta = 0°$ of grain D is missing because only a small part of this grain is included in the $\theta = 0°$ scanned region (see Figure 5a).

https://doi.org/10.1021/acs.jpcc.1c08533
J. Phys. Chem. C 2021, 125, 27996−28003

$$I(\theta) = y + B\cos(f\theta + \beta) \quad (2)$$

in which y denotes a θ-independent term, B the amplitude, f the reciprocal of the angular period, and β the phase along the θ-axis. This equation is identical with eq 1 in a mathematical sense but should be distinguished because it is a function of rotation angle θ and not ϕ, which is defined in the space-fixed coordinates. The parameters y, B, f, and β determined from fitting are given in Figure 6. What we directly noticed is that these parameters are all near in value regardless of the grain, except for phase β. The varying phase β indicates that the grains in the BA_2PbI_4 film have orientations different from each other. To refine eq 2 based on this finding, we imposed two constraints that stemmed from physical requirements. First, the area intensity I must be nonnegative, so $y \geq B$. The averages of y and B for the six grains are 0.47 ($\pm$0.03) and 0.49 ($\pm$0.03), respectively; we thus took $y = B = 0.48$. Second, because of the symmetry of the PbI_6 octahedra, the θ dependence is expected to have period 90°, that is, $f = \pi/45 = 0.070$ (recall our analysis of the ϕ dependence in Figure 3b). The new model function that results from the above constraints is written as

$$I'(\theta) = 0.48 + 0.48\cos(0.070\theta + \beta') \quad (3)$$

We refit the dependence on θ by using eq 3; the results are shown as solid lines in Figure 6. The agreement between the observed intensities and the fits somewhat deteriorates, particularly for grains A, C, and D, because of only one fitting parameter β' in eq 3 but is overall satisfactory.

The final step of our mapping of grain orientation is to convert the intensity of line 6 observed in the thin film to the orientation of the PbI_6 octahedra (i.e., angle ϕ). To explain how this step is done, we take film orientation $\theta = 40°$ as an example. The observed intensities of line 6 (closed circles in Figure S5a) were fitted to eq 3; the estimated values (open circles in Figure S5a) were obtained. Subsequently, to find $|\phi|$ ($0° \leq |\phi| \leq 45°$), the estimated values of I' were substituted into

$$|\phi| = \left| \frac{1}{0.070}\left[\cos^{-1}\left(\frac{I' - 0.48}{0.48}\right) - 3.12\right]\right| \quad (4)$$

Here phase 3.12 rad (= 179.0°) was taken from the fitted result of line 6 shown in Figure 3b. This means substitution of α into β', which corresponds to a conversion to the space-fixed coordinates (see Figure S5b). The orientation of the octahedral lattice with respect to the Y-axis ($+\alpha$ vs $-\alpha$; see Figure S3a) was then determined on examining whether further counterclockwise rotation from 40° (i.e., increasing θ) increased the area intensity (Figure S3b). In the case of grain A, eq 3 with $\theta = 40°$ and $\beta' = 113°$ (Figure 6a) yielded $I' = 0.509$. On substituting this value into eq 4, we obtained $|\phi| = 23°$. As is discernible in Figure 6a, the cosine curve representing the dependence on θ of the intensity of line 6 for grain A has a positive slope at $\theta = 40°$; we concluded that the octahedral lattice of grain A is tilted by +23° and not −23° with respect to the Y-axis. The orientations of other grains were obtained similarly. The result of our mapping of grain orientation of a BA_2PbI_4 thin film is shown schematically in Figure 7. The determined orientations are believed to be uniform inside the grains (see the small error bars in Figure 6) but could be different near the boundaries.

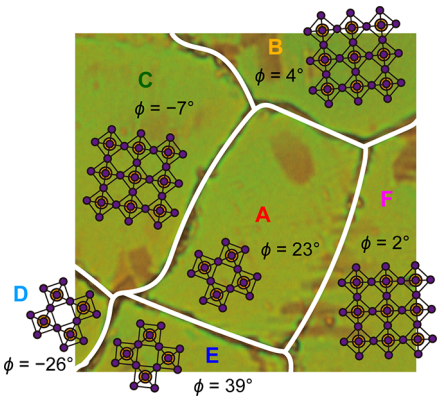

Figure 7. Result of mapping of grain orientation of a BA_2PbI_4 thin film derived from LFPR imaging. The orientation of each grain is shown schematically with a tilted PbI_6 octahedral lattice, with the obtained value of ϕ.

CONCLUSIONS

In this work, we demonstrated mapping of grain orientation of a BA_2PbI_4 thin film using LFPR microspectroscopy. Similar mapping is also possible by using the vibrational modes of the BA^+ cation with proper symmetry,[25] but they are at least an order of magnitude weaker in intensity than the LF phonon modes, so the mapping would take a much longer time. Unlike EBSD, which can probe only regions of a grain within ~50 nm from the surface, our approach as an optical technique is applicable to deeper regions, such as a 2D perovskite layer between electron- and hole-transport layers in photovoltaic devices. Furthermore, neither sophisticated sample pretreatment nor high vacuum is required, making mapping under ambient conditions feasible. One limitation of the present method is that it cannot be directly extended to 3D orientation mapping[24] of 3D perovskites, for which LFPR experiments must be performed not only in $Z(YY)Z$ but also in all other possible polarization configurations. Although this work is a case study of BA_2PbI_4, a 2D perovskite that tends to grow horizontally on the substrate, we can also achieve mapping of grain orientation of 2D perovskites having another cation[7,14] (e.g., PEA_2PbI_4; PEA = phenethylammonium) and those that prefer vertical orientation, such as $BA_2MA_{n-1}Pb_nI_{3n+1}$ ($n \geq 4$; MA = methylammonium).[12,13] The results presented here provide a basis for future studies of grain orientation *in situ* of 2D and 3D perovskites.

ASSOCIATED CONTENT

Supporting Information

The Supporting Information is available free of charge at https://pubs.acs.org/doi/10.1021/acs.jpcc.1c08533.

Peak positions and line widths of six Gaussian lines (Table S1); photographs of crystal and thin-film samples of BA_2PbI_4 (Figure S1); schematic of the confocal Raman microspectrometer (Figure S2); determination of two orientations that produce the same line intensity (Figure S3); ROI used to calculate the average of the intensity of line 6 for each grain (Figure S4); and illustration of relation of θ to ϕ (Figure S5) (PDF)

https://doi.org/10.1021/acs.jpcc.1c08533
J. Phys. Chem. C 2021, 125, 27996−28003

AUTHOR INFORMATION

Corresponding Author

Shinsuke Shigeto − *Department of Chemistry, Graduate School of Science and Technology, Kwansei Gakuin University, Sanda, Hyogo 669-1337, Japan;* orcid.org/0000-0002-2035-2068; Email: shigeto@kwansei.ac.jp

Authors

Shogo Toda − *Department of Chemistry, Graduate School of Science and Technology, Kwansei Gakuin University, Sanda, Hyogo 669-1337, Japan*

Eric Wei-Guang Diau − *Department of Applied Chemistry, Institute of Molecular Science, and Center for Emergent Functional Matter Science, National Yang Ming Chiao Tung University, Hsinchu 30010, Taiwan;* orcid.org/0000-0001-6113-5679

Complete contact information is available at: https://pubs.acs.org/10.1021/acs.jpcc.1c08533

Notes

The authors declare no competing financial interest.

ACKNOWLEDGMENTS

We thank Dr. V. Kattoor and Dr. E. Jokar for preparation of the 2D perovskite materials. This work was supported by JSPS KAKENHI Grants JP19H02821 (S.S.) and JP18J20312 (S.T.), Ministry of Science and Technology, Taiwan (Grants MOST 110-2123-M-A49-001 and MOST 110-2634-F-009-026 (E.D.)), and the Center for Emergent Functional Matter Science of National Yang Ming Chiao Tung University (NYCU) from The Featured Areas Research Center Program within the framework of the Higher Education SPROUT Project by the Ministry of Education (MOE) in Taiwan (E.D.).

REFERENCES

(1) Saidaminov, M. I.; Mohammed, O. F.; Bakr, O. M. Low-Dimensional-Networked Metal Halide Perovskites: The Next Big Thing. *ACS Energy Lett.* **2017**, *2*, 889−896.

(2) Ortiz-Cervantes, C.; Carmona-Monroy, P.; Solis-Ibarra, D. Two-Dimensional Halide Perovskites in Solar Cells: 2D or Not 2D? *ChemSusChem* **2019**, *12*, 1560−1575.

(3) Grancini, G.; Nazeeruddin, M. K. Dimensional Tailoring of Hybrid Perovskites for Photovoltaics. *Nat. Rev. Mater.* **2019**, *4*, 4−22.

(4) Mao, L.; Stoumpos, C. C.; Kanatzidis, M. G. Two-Dimensional Hybrid Halide Perovskites: Principles and Promises. *J. Am. Chem. Soc.* **2019**, *141*, 1171−1190.

(5) Zhang, F.; Lu, H.; Tong, J.; Berry, J. J.; Beard, M. C.; Zhu, K. Advances in Two-Dimensional Organic−Inorganic Hybrid Perovskites. *Energy Environ. Sci.* **2020**, *13*, 1154−1186.

(6) Smith, I. C.; Hoke, E. T.; Solis-Ibarra, D.; McGehee, M. D.; Karunadasa, H. I. A Layered Hybrid Perovskite Solar-Cell Absorber with Enhanced Moisture Stability. *Angew. Chem., Int. Ed.* **2014**, *53*, 11232−11235.

(7) Quintero-Bermudez, R.; Gold-Parker, A.; Proppe, A. H.; Munir, R.; Yang, Z.; Kelley, S. O.; Amassian, A.; Toney, M. F.; Sargent, E. H. Compositional and Orientational Control in Metal Halide Perovskites of Reduced Dimensionality. *Nat. Mater.* **2018**, *17*, 900−907.

(8) Kamminga, M. E.; Fang, H.-H.; Filip, M. R.; Giustino, F.; Baas, J.; Blake, G. R.; Loi, M. A.; Palstra, T. T. M. Confinement Effects in Low-Dimensional Lead Iodide Perovskite Hybrids. *Chem. Mater.* **2016**, *28*, 4554−4562.

(9) Blancon, J. C.; Stier, A. V.; Tsai, H.; Nie, W.; Stoumpos, C. C.; Traoré, B.; Pedesseau, L.; Kepenekian, M.; Katsutani, F.; Noe, G. T.; et al. Scaling Law for Excitons in 2D Perovskite Quantum Wells. *Nat. Commun.* **2018**, *9*, 2254.

(10) Zhu, X.; Xu, Z.; Zuo, S.; Feng, J.; Wang, Z.; Zhang, X.; Zhao, K.; Zhang, J.; Liu, H.; Priya, S.; et al. Vapor-Fumigation for Record Efficiency Two-Dimensional Perovskite Solar Cells with Superior Stability. *Energy Environ. Sci.* **2018**, *11*, 3349−3357.

(11) Liu, P.; Han, N.; Wang, W.; Ran, R.; Zhou, W.; Shao, Z. High-Quality Ruddlesden−Popper Perovskite Film Formation for High-Performance Perovskite Solar Cells. *Adv. Mater.* **2021**, *33*, 2002582.

(12) Cao, D. H.; Stoumpos, C. C.; Farha, O. K.; Hupp, J. T.; Kanatzidis, M. G. 2D Homologous Perovskites as Light-Absorbing Materials for Solar Cell Applications. *J. Am. Chem. Soc.* **2015**, *137*, 7843−7850.

(13) Chen, A. Z.; Shiu, M.; Ma, J. H.; Alpert, M. R.; Zhang, D.; Foley, B. J.; Smilgies, D.-M.; Lee, S.-H.; Choi, J. J. Origin of Vertical Orientation in Two-Dimensional Metal Halide Perovskites and Its Effect on Photovoltaic Performance. *Nat. Commun.* **2018**, *9*, 1336.

(14) Yuan, M.; Quan, L. N.; Comin, R.; Walters, G.; Sabatini, R.; Voznyy, O.; Hoogland, S.; Zhao, Y.; Beauregard, E. M.; Kanjanaboos, P.; et al. Perovskite Energy Funnels for Efficient Light-Emitting Diodes. *Nat. Nanotechnol.* **2016**, *11*, 872−877.

(15) Wang, K.; Wu, C.; Jiang, Y.; Yang, D.; Wang, K.; Priya, S. Distinct Conducting Layer Edge States in Two-Dimensional (2D) Halide Perovskite. *Sci. Adv.* **2019**, *5*, eaau3241.

(16) McDonald, S. A.; Reischig, P.; Holzner, C.; Lauridsen, E. M.; Withers, P. J.; Merkle, A. P.; Feser, M. Non-Destructive Mapping of Grain Orientations in 3D by Laboratory X-Ray Microscopy. *Sci. Rep.* **2015**, *5*, 14665.

(17) Larson, B. C.; Yang, W.; Ice, G. E.; Budai, J. D.; Tischler, J. Z. Three-Dimensional X-Ray Structural Microscopy with Submicrometre Resolution. *Nature* **2002**, *415*, 887−890.

(18) Liu, H. H.; Schmidt, S.; Poulsen, H. F.; Godfrey, A.; Liu, Z. Q.; Sharon, J. A.; Huang, X. Three-Dimensional Orientation Mapping in the Transmission Electron Microscope. *Science* **2011**, *332*, 833−834.

(19) Schmidt, S.; Larsen, P.; Huang, X. 3D Grain Orientation Mapping of Nanocrystalline Materials in the TEM. *Acta Crystallogr., Sect. A: Found. Adv.* **2014**, *70*, C735.

(20) Wilkinson, A. J.; Britton, T. B. Strains, Planes, and Ebsd in Materials Science. *Mater. Today* **2012**, *15*, 366−376.

(21) Wu, G.; Zhu, W.; He, Q.; Feng, Z.; Huang, T.; Zhang, L.; Schmidt, S.; Godfrey, A.; Huang, X. 2D and 3D Orientation Mapping in Nanostructured Metals: A Review. *Nano Mater. Sci.* **2020**, *2*, 50−57.

(22) Nowell, M. M.; Witt, R. A.; True, B. W. EBSD Sample Preparation: Techniques, Tips, and Tricks. *Microsc. Today* **2005**, *13*, 44−49.

(23) Tesar, K.; Gregora, I.; Beresova, P.; Vanek, P.; Ondrejkovic, P.; Hlinka, J. Raman Scattering Yields Cubic Crystal Grain Orientation. *Sci. Rep.* **2019**, *9*, 9385.

(24) Ilchenko, O.; Pilgun, Y.; Kutsyk, A.; Bachmann, F.; Slipets, R.; Todeschini, M.; Okeyo, P. O.; Poulsen, H. F.; Boisen, A. Fast and Quantitative 2D and 3D Orientation Mapping Using Raman Microscopy. *Nat. Commun.* **2019**, *10*, 5555.

(25) Toda, S.; Yanagita, N.; Jokar, E.; Diau, E. W.-G.; Shigeto, S. Inter- and Intragrain Inhomogeneity in 2D Perovskite Thin Films Revealed by Relative Grain Orientation Imaging Using Low-Frequency Polarized Raman Microspectroscopy. *J. Phys. Chem. Lett.* **2020**, *11*, 3871−3876.

(26) McMeekin, D. P.; Sadoughi, G.; Rehman, W.; Eperon, G. E.; Saliba, M.; Hörantner, M. T.; Haghighirad, A.; Sakai, N.; Korte, L.; Rech, B.; et al. A Mixed-Cation Lead Mixed-Halide Perovskite Absorber for Tandem Solar Cells. *Science* **2016**, *351*, 151−155.

(27) Xu, F.; Zhang, T.; Li, G.; Zhao, Y. Mixed Cation Hybrid Lead Halide Perovskites with Enhanced Performance and Stability. *J. Mater. Chem. A* **2017**, *5*, 11450−11461.

(28) Grancini, G.; Roldán-Carmona, C.; Zimmermann, I.; Mosconi, E.; Lee, X.; Martineau, D.; Narbey, S.; Oswald, F.; De Angelis, F.; Graetzel, M.; et al. One-Year Stable Perovskite Solar Cells by 2D/3D Interface Engineering. *Nat. Commun.* **2017**, *8*, 15684.

(29) Stoumpos, C. C.; Cao, D. H.; Clark, D. J.; Young, J.; Rondinelli, J. M.; Jang, J. I.; Hupp, J. T.; Kanatzidis, M. G. Ruddlesden−Popper Hybrid Lead Iodide Perovskite 2D Homologous Semiconductors. *Chem. Mater.* **2016**, *28*, 2852−2867.
(30) Kattoor, V.; Awasthi, K.; Jokar, E.; Diau, E. W.-G.; Ohta, N. Integral Method Analysis of Electroabsorption Spectra and Electrophotoluminescence Study of $(C_4H_9NH_3)_2PbI_4$ Organic−Inorganic Quantum Well. *J. Phys. Chem. C* **2018**, *122*, 26623−26634.
(31) Liu, J.; Gao, C.; He, X.; Ye, Q.; Ouyang, L.; Zhuang, D.; Liao, C.; Mei, J.; Lau, W. Improved Crystallization of Perovskite Films by Optimized Solvent Annealing for High Efficiency Solar Cell. *ACS Appl. Mater. Interfaces* **2015**, *7*, 24008−24015.
(32) Matsuda, A.; Sakaguchi, N.; Shigeto, S. Can Cells Maintain Their Bioactivity in Ionic Liquids? A Novel Single-Cell Assessment by Raman Microspectroscopy. *J. Raman Spectrosc.* **2019**, *50*, 768−777.
(33) Chang, C.-F.; Wang, S.-C.; Shigeto, S. In Situ Ultralow-Frequency Raman Tracking of the Polymorphic Transformation of Crystalline 1,1′-Binaphthyl. *J. Phys. Chem. C* **2014**, *118*, 2702−2709.
(34) Chang, C.-F.; Okajima, H.; Hamaguchi, H.; Shigeto, S. Imaging Molecular Crystal Polymorphs and Their Polycrystalline Microstructures in Situ by Ultralow-Frequency Raman Spectroscopy. *Chem. Commun.* **2014**, *50*, 12973−12976.
(35) Yoshikawa, Y.; Shigeto, S. A Simple Calibration Method of Anti-Stokes−Stokes Raman Intensity Ratios Using the Water Spectrum for Intracellular Temperature Measurements. *Appl. Spectrosc.* **2020**, *74*, 1295−1296.
(36) Damen, T. C.; Porto, S. P. S.; Tell, B. Raman Effect in Zinc Oxide. *Phys. Rev.* **1966**, *142*, 570−574.
(37) Huang, C.-K.; Hamaguchi, H.; Shigeto, S. *In Vivo* Multimode Raman Imaging Reveals Concerted Molecular Composition and Distribution Changes During Yeast Cell Cycle. *Chem. Commun.* **2011**, *47*, 9423−9425.
(38) Uzunbajakava, N.; Lenferink, A.; Kraan, Y.; Volokhina, E.; Vrensen, G.; Greve, J.; Otto, C. Nonresonant Confocal Raman Imaging of DNA and Protein Distribution in Apoptotic Cells. *Biophys. J.* **2003**, *84*, 3968−3981.
(39) van Manen, H.-J.; Kraan, Y. M.; Roos, D.; Otto, C. Intracellular Chemical Imaging of Heme-Containing Enzymes Involved in Innate Immunity Using Resonance Raman Microscopy. *J. Phys. Chem. B* **2004**, *108*, 18762−18771.
(40) Dhanabalan, B.; Leng, Y.-C.; Biffi, G.; Lin, M.-L.; Tan, P.-H.; Infante, I.; Manna, L.; Arciniegas, M. P.; Krahne, R. Directional Anisotropy of the Vibrational Modes in 2D-Layered Perovskites. *ACS Nano* **2020**, *14*, 4689−4697.
(41) Billing, D. G.; Lemmerer, A. Synthesis, Characterization and Phase Transitions in the Inorganic-Organic Layered Perovskite-Type Hybrids $[(C_nH_{2n+1}NH_3)_2PbI_4]$, n = 4, 5 and 6. *Acta Crystallogr., Sect. B: Struct. Sci.* **2007**, *63*, 735−747.
(42) Sheikh, T.; Nag, A. Mn Doping in Centimeter-Sized Layered 2D Butylammonium Lead Bromide (BA_2PbBr_4) Single Crystals and Their Optical Properties. *J. Phys. Chem. C* **2019**, *123*, 9420−9427.
(43) Mauck, C. M.; France-Lanord, A.; Hernandez Oendra, A. C.; Dahod, N. S.; Grossman, J. C.; Tisdale, W. A. Inorganic Cage Motion Dominates Excited-State Dynamics in 2D-Layered Perovskites $(C_xH_{2x+1}NH_3)_2PbI_4$ (x = 4−9). *J. Phys. Chem. C* **2019**, *123*, 27904−27916.
(44) Pérez-Osorio, M. A.; Lin, Q.; Phillips, R. T.; Milot, R. L.; Herz, L. M.; Johnston, M. B.; Giustino, F. Raman Spectrum of the Organic−Inorganic Halide Perovskite $CH_3NH_3PbI_3$ from First Principles and High-Resolution Low-Temperature Raman Measurements. *J. Phys. Chem. C* **2018**, *122*, 21703−21717.

https://doi.org/10.1021/acs.jpcc.1c08533
J. Phys. Chem. C 2021, 125, 27996−28003